Inorg. Chem. **2003**, *42*, 1973–1981

The Crystal Structure and Magnetic Properties of a New Ferrimagnetic Semiconductor: $Ca_{21}Mn_4Sb_{18}$

Aaron P. Holm, Marilyn M. Olmstead, and Susan M. Kauzlarich*

Department of Chemistry, University of California, One Shields Avenue, Davis, California 95616

Received September 3, 2002

Single crystals of the new transition metal Zintl phase, $Ca_{21}Mn_4Sb_{18}$, were prepared by high temperature melt synthesis. The crystal structure was determined by single crystal X-ray diffraction to be monoclinic in the space group *C*2/*c*. Crystal information was obtained at 90 K, and unit cell parameters were determined ($a = 17.100(2)$ Å, $b = 17.073(2)$ Å, $c = 16.857(2)$ Å, $\beta = 92.999(2)°$, $Z = 2$, R1 = 0.0540, wR2 = 0.1437). The structure can be described as containing 4 discreet units per formula unit: 1 linear $[Mn_4Sb_{10}]^{22-}$ anion, 2 dumbbell-shaped $[Sb_2]^{4-}$ anions, 4 individual Sb^{3-} anions, and 21 Ca^{2+} cations. The $[Mn_4Sb_{10}]^{22-}$ anion contains four edge-shared $MnSb_4$ tetrahedra with distances between Mn ions of 3.388(4) Å, 2.782(4) Å, and 2.760(4) Å. Electron counting suggests that the Mn are 2+. Temperature dependent magnetization shows a ferromagnetic-like transition temperature at ~52 K which is suppressed with increasing magnetic field. The paramagnetic regime is best fit to a ferrimagnetic model, providing a total effective moment of 4.04(2) μ_B, significantly less than that expected for 4 Mn^{2+} ions (11.8 μ_B). Temperature dependent resistivity shows that this compound is a semiconductor with an activation energy of 0.159(2) eV (100–300 K).

Introduction

The preparation of intermetallic compounds possessing a combination of electropositive and electronegative elements has introduced a rich variety of solid state structures due to the tendency for the electronegative atoms to form varying degrees of localized, covalently bonding, polyanionic networks.[1] Generally, these systems obey classical Zintl–Klemm electron counting rules with closed-shell electronic configurations due to complete charge transfer from a noble metal (groups 1 and 2) or rare-earth element to a post-transition metal element (groups 13–15).[2] With the introduction of transition metal elements, comparable electronegativities and a variation in oxidation states introduce additional complexity in the electronic structure that can lead to interesting magnetic and electronic properties in these systems.

The motivation for investigating new Zintl phases lies not only in their potential for offering new structure types and unique bonding arrangements but also in their possible materials applications. Recent reports on the new thermoelectric materials, $CsBi_4Te_6$ and $Ba_4In_8Sb_{16}$, pointed to the unusual combination of complex electrical, structural, and thermal properties as a source for the high thermoelectric figure of merits reported.[3,4] In addition, the rare-earth gallium antimonide, $La_{13}Ga_8Sb_{21}$, displays a superconducting transition at $T_c = 2.4$ K opening up the possibility for other Zintl compounds with complex bonding arrangements and low electronegativity differences between component atoms to be superconductors.[5] Zintl phases also have potential in the burgeoning field of molecule-based magnets where the solid state structures of these magnets consist of arrays of molecular units similar to the typical Zintl phase.[6,7] The complexity inherent in the electronic and crystal structures of Zintl phases has produced much interest and discovery of new compounds with large magnetoresistance effects,

* To whom correspondence should be addressed. E-mail: smkauzlarich@ucdavis.edu.

(1) Eisenmann, B.; Cordier, G. In *Chemistry, Structure, and Bonding of Zintl Phases and Ions*; Kauzlarich, S. M., Ed.; VCH Publishers: New York, 1996; p 61.
(2) *Chemistry, Structure, and Bonding of Zintl Phases and Ions*; Kauzlarich, S. M., Ed.; VCH Publishers: New York, 1996.
(3) Kim, S.-J.; Hu, S.; Uher, C.; Kanatzidis, M. G. *Chem. Mater.* **1999**, *11*, 3154–3159.
(4) Chung, D.-Y.; Hogan, T.; Brazis, P.; Rocci-Lane, M.; Kannewurf, C.; Bastea, M.; Uher, C.; Kanatzidis, M. G. *Science* **2000**, *287*, 1024–1027.
(5) Mills, A. M.; Deakin, L.; Mar, A. *Chem. Mater.* **2001**, *13*, 1778–1788.
(6) Holmes, S. M.; Girolami, G. S. *J. Am. Chem. Soc.* **1999**, *121*, 5593–5594.
(7) Miller, J. S.; Epstein, A. J. *Chem. Eng. News* **1995**, *73*, 30–41.

10.1021/ic020530r CCC: $25.00
Published on Web 02/14/2003

most notably in the $A_{14}MnPn_{11}$ (A = Ca, Sr, Ba, Eu, Yb; Pn = P, As, Sb, Bi) series of compounds where colossal magnetoresistance has been reported.[2,8−34] This potential for preparing unique compounds at the metal−insulator boundary and the relationship to other correlated electron systems have motivated our investigations of transition metal containing ternary systems, specifically manganese containing antimonides.

A new structure type belonging to the family of Mn containing transition metal Zintl phases with formula $Ca_{21}Mn_4Sb_{18}$ has been synthesized by high temperature melt synthesis. This structure complements the recently reported $Sr_{21}Mn_4Sb_{18}$ phase that is compositionally identical but differs substantially in its structure.[35] $Ca_{21}Mn_4Sb_{18}$ is a unique structure type containing noninfinite, discrete linear units of Mn-centered, edge sharing tetrahedral units in a $[Mn_4Sb_{10}]^{22-}$ unit. It is also a new Zintl phase retaining the well-known $[Sb_2]^{4-}$ Zintl anion, exhibiting a consistency within the cationic framework with other Zintl phases possessing this anionic unit.[36−45] In addition, the structure contains isolated Sb^{3-} anions that are arranged in an analogous sequence to other Zintl phases containing both of these anionic units in relation to both the anionic structure and the cationic structure.[36−45] Magnetic and electronic properties are also reported and are discussed in light of the reported structure.

Experimental Section

Synthesis. Single crystals of $Ca_{21}Mn_4Sb_{18}$ were produced by a high temperature melt synthesis using Sn as a flux.[46] Elemental Ca (Alfa, 99.987%), Mn pieces (Alfa, 99.98%), Sb shot (CERAC, 99.999%), and Sn shot (Alfa, 99.99%) were handled in a N_2 filled drybox. The mass of each element was scaled to 3.5 g of Sn according to the ratio 21Ca/7Mn/18Sb/64Sn. Approximately half of the Sn was placed in a 2 mL alumina crucible, followed by Ca, Mn, Sb, and the remaining Sn. The crucible, fit with a small plug of quartz wool, was placed in a quartz tube that was flattened on one end. A second crucible was tightly filled with quartz wool and inverted on top of the first. An additional plug of quartz wool was placed on top of the crucibles, and the quartz tube was sealed under $^1/_5$ atm of argon. The reaction vessel was placed upright in a box furnace and heated at 3 °C/hr to 950 °C, maintained at 950 °C for 1 h, and then cooled at 3 °C/hr to 800 °C where it remained for 7 days. It was removed at 800 °C, inverted, and immediately placed in a centrifuge and spun for one minute at 7500 rpm. The reaction was opened in a N_2 filled drybox equipped with a microscope and at moisture levels <1 ppm. The crucible initially containing the elements was filled with a mixture of large amounts of multifaceted, highly reflective crystals of $Ca_{21}Mn_4Sb_{18}$ and a small amount of Sn powder. The second crucible contained a solid block of Sn separated from the crystalline material during the centrifuge process. Initial attempts to synthesize this material resulted in mixtures of $Ca_{21}Mn_4Sb_{18}$ and $Ca_{14}MnSb_{11}$ crystals, but after extensive synthetic optimization, a pure phase of $Ca_{21}Mn_4Sb_{18}$ was obtained according to the parameters given.

Elemental Analysis. Quantitative elemental analysis of $Ca_{21}Mn_4Sb_{18}$ was performed using a Cameca SX50 electron microprobe with a wavelength dispersive spectrometer. The microprobe was operated at 15 keV accelerating potential and 10 nA beam current. The elemental analysis was based on 17 spots (spot size 1 μm) from three crystals. The Ca, Mn, Sb, and Sn content were determined using elemental Ca as a standard. The elemental stoichiometry was quantitatively determined to be $Ca_{21.0(0)}Mn_{4.01(1)}Sb_{18.0(1)}Sn_{0.099(13)}$. The negligible amount of Sn is attributed to flux not completely removed in the centrifuge process.

(8) Brock, S. L.; Weston, L. J.; Olmstead, M. M.; Kauzlarich, S. M. *J. Solid State Chem.* **1993**, *107*, 513−523.
(9) Chan, J. Y.; Kauzlarich, S. M.; Klavins, P.; Shelton, R. N.; Webb, D. J. *Chem. Mater.* **1997**, *9*, 3132−3135.
(10) Chan, J. Y.; Olmstead, M. M.; Kauzlarich, S. M.; Webb, D. J. *Chem. Mater.* **1997**, *10*, 3583−3588.
(11) Chan, J. Y.; Wang, M. E.; Rehr, A.; Kauzlarich, S. M.; Webb, D. J. *Chem. Mater.* **1997**, *9*, 2131−2138.
(12) Chan, J. Y.; Kauzlarich, S. M.; Klavins, P.; Shelton, R. N.; Webb, D. J. *Phys. Rev. B* **1998**, *57*, 8103−8106.
(13) Chan, J. Y.; Kauzlarich, S. M.; Klavins, P.; Liu, J.-Z.; Shelton, R. N.; Webb, D. J. *Phys. Rev. B* **2000**, *61*, 459−463.
(14) Del Castillo, J.; Webb, D. J.; Kauzlarich, S. M.; Kuromoto, T. Y. *Phys. Rev. B* **1993**, *47*, 4849−4852.
(15) Fisher, I. R.; Wiener, T. A.; Bud'ko, S. L.; Canfield, P. C.; Chan, J. Y.; Kauzlarich, S. M. *Phys. Rev. B* **1999**, *59*, 13829−13834.
(16) Fisher, I. R.; Bud'ko, S. L.; Song, C.; Canfield, P. C.; Ozawa, T. C.; Kauzlarich, S. M. *Phys. Rev. Lett.* **2000**, *85*, 1120−1123.
(17) Gallup, R. F.; Fong, C. Y.; Kauzlarich, S. M. *Inorg. Chem.* **1992**, *31*, 115−118.
(18) Holm, A. P.; Kauzlarich, S. M.; Morton, S. A.; Waddill, G. D.; Pickett, W. E.; Tobin, J. G. *J. Am. Chem. Soc.* **2002**, *124*, 9894−9898.
(19) Kauzlarich, S. M.; Kuromoto, T. Y.; Olmstead, M. M. *J. Am. Chem. Soc.* **1989**, *111*, 8041−8042.
(20) Kauzlarich, S. M.; Kuromoto, T. Y. *Croat. Chem. Acta* **1991**, *64*, 343−352.
(21) Kauzlarich, S. M.; Thomas, M. M.; Odink, D. A.; Olmstead, M. M. *J. Am. Chem. Soc.* **1991**, *113*, 7205−7208.
(22) Kauzlarich, S. M.; Payne, A. C.; Webb, D. J. In *Magnetism: Molecules to Materials III*; Miler, J. S., Drillon, M., Eds.; Wiley-VCH: Weinham, 2002; pp 37−62.
(23) Kim, H.; Chan, J. Y.; Olmstead, M. M.; Klavins, P.; Webb, D. J.; Kauzlarich, S. M. *Chem. Mater.* **2002**, *14*, 206−216.
(24) Kuromoto, T. Y.; Kauzlarich, S. M.; Webb, D. J. *Mol. Cryst. Liq. Cryst.* **1989**, *181*, 349−357.
(25) Kuromoto, T. Y.; Kauzlarich, S. M.; Webb, D. J. *Chem. Mater.* **1992**, *4*, 435−440.
(26) Payne, A. C.; Olmstead, M. M.; Kauzlarich, S. M.; Webb, D. J. *Chem. Mater.* **2001**, *13*, 1398−1406.
(27) Rehr, A.; Kauzlarich, S. M. *J. Alloys Compd.* **1994**, *207*, 424−426.
(28) Rehr, A.; Kuromoto, T. Y.; Kauzlarich, S. M.; Del Castillo, J.; Webb, D. J. *Chem. Mater.* **1994**, *6*, 93−99.
(29) Sánchez-Portal, D.; Martin, R. M.; Kauzlarich, S. M.; Pickett, W. E. *Phys. Rev. B* **2002**, *65*, 144411−144415. (See p 144414.)
(30) Siemens, D. P.; Del Castillo, J.; Potter, W.; Webb, D. J.; Kuromoto, T. Y.; Kauzlarich, S. M. *Solid State Commun.* **1992**, *84*, 1029−1031.
(31) Webb, D. J.; Kuromoto, T. Y.; Kauzlarich, S. M. *J. Magn. Magn. Mater.* **1991**, *98*, 71−75.
(32) Webb, D. J.; Kuromoto, T. Y.; Kauzlarich, S. M. *J. Appl. Phys.* **1991**, *69*, 4825.
(33) Webb, D. J.; Cohen, R.; Klavins, P.; Shelton, R. N.; Chan, J. Y.; Kauzlarich, S. M. *J. Appl. Phys.* **1998**, *83*, 7192−7194.
(34) Young, D. M.; Torardi, C. C.; Olmstead, M. M.; Kauzlarich, S. M. *Chem. Mater.* **1995**, *7*, 93−101.
(35) Kim, H.; Condron, C. L.; Holm, A. P.; Kauzlarich, S. M. *J. Am. Chem. Soc.* **2000**, *122*, 10720−10721.
(36) Eisenmann, B.; Gieck, C.; Röbler, U. *Z. Anorg. Allg. Chem.* **1999**, *625*, 1331−1336.
(37) Cordier, G.; Schäfer, H.; Stelter, M. *Z. Naturforsch.* **1985**, *40b*, 868−871.
(38) Papoian, G. A.; Hoffman, R. *J. Solid State Chem.* **1998**, *139*, 8−21.
(39) Papoian, G. A.; Hoffman, R. *Angew. Chem., Int. Ed.* **2000**, *39*, 2408−2448.
(40) von Schnering, H. G. *Angew. Chem., Int. Ed. Engl.* **1981**, *20*, 33−51.
(41) von Schnering, H. G.; Hönle, W. *Chem. Rev.* **1988**, *88*, 243−273.
(42) Schäfer, H.; Eisenmann, B.; Müller, W. *Angew. Chem., Int. Ed. Engl.* **1973**, *12*, 694−712.
(43) Wang, B. Y.; Calvert, L. D.; Gabe, E. J.; Taylor, J. B. *Acta Crystallogr.* **1978**, *B34*, 1962−1965.
(44) Vidyasagar, K.; Hönle, W.; von Schnering, H. G. *J. Alloys Compd.* **1996**, *235*, 37−40.
(45) Hönle, W.; Lin, J.; Hartweg, M.; von Schnering, H. G. *J. Solid State Chem.* **1992**, *97*, 1−9.
(46) Canfield, P. C.; Fisk, Z. *Philos. Mag. B* **1992**, *65*, 1117−1123.

Single Crystal X-ray Diffraction. The reaction produced a high yield of reflective, dark, multifacetted single crystals with crystal faces ranging in approximate dimension from 0.05 mm^2 to 1.0 mm^2. A suitable crystal was coated with Paratone N oil and subsequently mounted on a glass fiber under a nitrogen cold stream. The single crystal diffraction data was collected at 90 K using a Bruker SMART 1000 CCD diffractometer employing graphite monochromatized Mo Kα radiation ($\lambda = 0.71069$ Å). The SMART software was used for data acquisition, the SAINT software for data extraction and reduction, and the SADABS software for the empirical absorption correction. Initial atomic positions were found by direct methods using XS followed by subsequent difference Fourier syntheses. The refinement was performed by least-squares methods using SHELXL-97. Data collection parameters and crystallographic information are provided in Table 2. Positional parameters and isotropic thermal parameters are provided in Table 3. Complete crystallographic information in the form of a CIF formatted file is available as Supporting Information.

Magnetic Susceptibility Measurements. Direct current magnetization data were obtained utilizing a Quantum Design MPMS superconducting quantum interference device (SQUID) magnetometer with a 7.0 T superconducting magnet. Temperature dependent and field dependent magnetization measurements of the title compound were measured using a single crystal sample (0.00045 g) coated with N type Apiezon grease and placed in a straw. The temperature dependent data were obtained by measuring zero-field-cooled (ZFC) magnetization from 2 to 300 K and field-cooled (FC) magnetization from 300 to 2 K in magnetic fields from 100 to 50000 Oe. Field dependent magnetization data were taken at 2 K and 150K by sweeping through fields from 0 to 7 T, 7 to −7 T, and −7 to 7 T.

Resistivity Measurements. Temperature dependent resistivity measurements were obtained on a crystal ($1.06 \times 1.08 \times 0.72$ mm^3) using an in-line four-probe method. A Keithley Model 224 current source and a Keithley 181 nanovoltmeter were used to measure resistivity from 2 to 300 K. A constant current (1 μA) was applied to the sample through the two outer leads, and the voltage was measured across the two inner leads. Thermal voltages were minimized by reversal of the current bias. Resistivity data were obtained on a single crystal with Pt leads attached by Ag paint and cured by resistive heating. The sample exhibited ohmic behavior. Resistivity as a function of temperature was also measured with an applied field of 1 T to test for magnetoresistive effects. A negligible change was observed, and it was concluded that the sample was not magnetoresistive.

Results and Discussion

Synthesis. The title compound was first discovered while attempting to synthesize the Mn containing analogue of the $Ca_{11}MSb_9$ structure[37,47] by a sealed niobium tube vapor transport synthesis. A mixture of crystals of $Ca_{14}MnSb_{11}$, $Ca_{11}Sb_{10}$, and the title compound were identified. The stoichiometry of the title compound was incorrectly identified initially as $Ca_{20}Mn_5Sb_{18}$, and this incorrect identification led to further attempts to isolate the compound by using the element ratio 20:5:18 and varying the heating scheme of the reaction. The best results employing this synthetic method were obtained with the same elemental ratio and the following reaction scheme: heat from room temperature at 60 °C/h to 1300 °C, dwell for 72 h, cool at 5 °C/ h to 850 °C, and furnace cool to room temperature. The crystals produced using this method were not of high enough quality to obtain an accurate crystal structure; therefore, an alternative was employed in the Sn flux method. Table 1 provides the relevant reaction schemes employed to obtain the final optimized synthesis. The final dwell time proved to be the most important aspect in eliminating any impurity phases and producing the highest quality crystals. This scheme is reported in detail in the Experimental Section, and all structural analysis and properties measurements were performed on crystals produced following this scheme.

Table 1. Synthesis Optimization for $Ca_{21}Mn_4Sb_{18}$

reaction	element ratio (Ca/Mn/Sb/Sn)	reaction scheme	products
1	20/7/18/64	RT $\xrightarrow{3\ °C/h}$ 800 °C, dewll 1 day	$Ca_{21}Mn_4Sb_{18}$, $Ca_{14}MnSb_{11}$, $Ca_{11}Sb_{10}$
2	20/7/18/64	RT $\xrightarrow{3\ °C/h}$ 800 °C, dwell 3 days	$Ca_{21}Mn_4Sb_{18}$, $Ca_{14}MnSb_{11}$, $Ca_{11}Sb_{10}$
3	20/7/18/64	RT $\xrightarrow{3\ °C/h}$ 800 °C, dwell 7 days	$Ca_{21}Mn_4Sb_{18}$, $Ca_{14}MnSb_{11}$
4	20/7/18/64	RT $\xrightarrow{3\ °C/h}$ 950 °C (1 hr) $\xrightarrow{3\ °C/h}$ 800 °C, dwell 3 days	$Ca_{21}Mn_4Sb_{18}$, $Ca_{14}MnSb_{11}$, $Ca_{11}Sb_{10}$
5	20/7/18/64	RT $\xrightarrow{3\ °C/h}$ 950 °C (1 hr) $\xrightarrow{3\ °C/h}$ 800 °C, dwell 3 days	$Ca_{21}Mn_4Sb_{18}$, $Ca_{14}MnSb_{11}$
6	20/7/18/64	RT $\xrightarrow{3\ °C/h}$ 950 °C (1 hr) $\xrightarrow{3\ °C/h}$ 800 °C, dwell 7 days	$Ca_{21}Mn_4Sb_{18}$
7	21/7/18/64	RT $\xrightarrow{3\ °C/h}$ 950 °C (1 hr) $\xrightarrow{3\ °C/h}$ 800 °Cm dwell 3 days	$Ca_{21}Mn_4Sb_{18}$, $Ca_{14}MnSb_{11}$, $Ca_{11}Sb_{10}$
8	21/7/18/64	RT $\xrightarrow{3\ °C/h}$ 950 °C (1 hr) $\xrightarrow{3\ °C/h}$ 800 °C, dwell 1 days	$Ca_{21}Mn_4Sb_{18}$, $Ca_{14}MnSb_{11}$
9	21/7/18/64	RT $\xrightarrow{3\ °C/h}$ 950 °C (1 hr) $\xrightarrow{3\ °C/h}$ 800 °C, dwell 7 days	$Ca_{21}Mn_4Sb_{18}$

Structure. A view of the structure of $Ca_{21}Mn_4Sb_{18}$ is shown in a projection down the *b*-axis in Figure 1. This new compound displays a complex structure possessing 4 discreet units: 1 $[Mn_4Sb_{10}]^{22-}$ anion, 2 dumbbell shaped $[Sb_2]^{4-}$ anions, 4 isolated Sb^{3-} anions, and 21 Ca^{2+} cations. Charges are assigned by considering a simple Zintl model. Figure 1 shows how these units form an elaborate array of one-dimensional $[Mn_4Sb_{10}]^{22-}$ rows, and extended channels of alternating Sb^{3-} anions and $[Sb_2]^{4-}$ dumbbells. The structure develops from extended columns of isolated $[Mn_4Sb_{10}]^{22-}$ units that alternate with a similar anionic column consisting of the alternating Sb^{3-} and $[Sb_2]^{4-}$ units. Columns stack directly above one another in both the *a* and *c* axial directions.

What is remarkable about this system is how the initially unyielding complexity of this solid state structure can be resolved into the stacking of one basic geometric shape along the same axial direction. The large numbers of Ca atoms (a total of 42 per unit cell) are conveniently arranged into alternating rows of interwoven columns of bicapped trigonal prisms, and an Sb atom from either the dumbbell or the isolated anion centers all of these Ca polyhedra. This

(47) Young, D. M.; Kauzlarich, S. M. *Chem. Mater.* **1995**, *7*, 206−209.

Table 2. Crystal Data and Structure Refinement for $Ca_{21}Mn_4Sb_{18}$

empirical formula	$Ca_{21}Mn_4Sb_{18}$
fw	3252.94
T	90(2) K
cryst syst	monoclinic
space group	$C2/c$
unit cell dimensions[a]	$a = 17.1001(15)$ Å $b = 17.0734(15)$ Å $c = 16.8574(15)$ Å $\alpha = 90°$ $\beta = 92.999(2)°$ $\gamma = 90°$
V	4914.9(8) Å^3
Z	2
D(calcd)	4.396 Mg/m^3
abs coeff	12.886 mm^{-1}
F(000)	5752
cryst size	0.10 × 0.10 × 0.07 mm^3
θ range for data collection	1.69−31.50°
index ranges	$-25 \le h \le 25$, $-25 \le k \le 25$, $-24 \le l \le 24$
reflns collected	47825
indep reflns	7846 [R(int) = 0.0383]
completeness to $\theta = 31.50°$	95.9%
abs correction	empirical
max and min transm	0.4657 and 0.3590
refinement method	full-matrix least-squares on F^2
data/restraints/params	7846/0/197
GOF on F^2	1.194
final R indices [$I > 2\sigma(I)$][b]	R1 = 0.0540, wR2 = 0.1437
R indices (all data)[b]	R1 = 0.0598, wR2 = 0.1462
largest diff peak and hole	12.427 and −2.789 e·Å^{-3}

[a] Room-temperature lattice parameters obtained from Guinier powder diffraction: $a = 17.0472(64)$ Å, $b = 17.1159(68)$ Å, $c = 16.8169(73)$ Å. [b] $R1 = \sum||F_o| - |F_c||/\sum|F_o|$. $wR2 = [\sum[w(F_o^2 - F_c^2)^2]/\sum[w(F_o^2)^2]]^{1/2}$, $w^{-1} = [\sigma^2(F_o^2) + (0.0305P)^2 + 28.39P]$, where $P = [\max(F_o^2,0) + 2F_c^2]/3$.

Table 3. Atomic Coordinates (×10^4) and Equivalent Isotropic Displacement parameters (Å^2 × 10^3) for $Ca_{21}Mn_4Sb_{18}$[a]

	x	y	z	U(eq)
Sb(1)	−59(1)	−4405(1)	6047(1)	8(1)
Sb(2)	1275(1)	−2570(1)	7588(1)	8(1)
Sb(3)	−50(1)	−755(1)	6029(1)	10(1)
Sb(4)	1428(1)	770(1)	7522(1)	8(1)
Sb(5)	−97(1)	2628(1)	6224(1)	7(1)
Sb(6)	3243(1)	−2492(1)	9645(1)	6(1)
Sb(7)	2120(1)	−2506(1)	5747(1)	7(1)
Sb(8)	2416(1)	−12(1)	5000(1)	6(1)
Sb(9)	6766(1)	−665(1)	7456(1)	9(1)
Mn(1)	0	−3602(1)	7500	8(1)
Mn(2)	0	−1618(2)	7500	11(1)
Mn(3)	0	11(2)	7500	12(1)
Mn(4)	0	1628(2)	7500	9(1)
Ca(1)	3315(1)	−2434(1)	7597(1)	10(1)
Ca(2)	4020(1)	−866(1)	9351(1)	7(1)
Ca(3)	57(1)	−2587(1)	5766(1)	10(1)
Ca(4)	3178(1)	885(1)	8450(1)	8(1)
Ca(5)	3077(1)	1158(1)	6224(1)	12(1)
Ca(6)	1711(1)	−895(1)	6579(1)	9(1)
Ca(7)	1877(1)	1266(1)	3815(1)	9(1)
Ca(8)	3627(1)	−1174(1)	5677(1)	10(1)
Ca(9)	1323(1)	−1330(1)	4364(1)	10(1)
Ca(10)	880(1)	912(1)	5703(1)	8(1)
Ca(11)	5000	−732(2)	7500	11(1)

[a] U(eq) is defined as one-third of the trace of the orthogonalized U^{ij} tensor.

geometric shape, and its preference to form interconnected networks, is seen in many pnicogen containing systems and in some non-pnictide containing systems.[48] The U_3Si_2

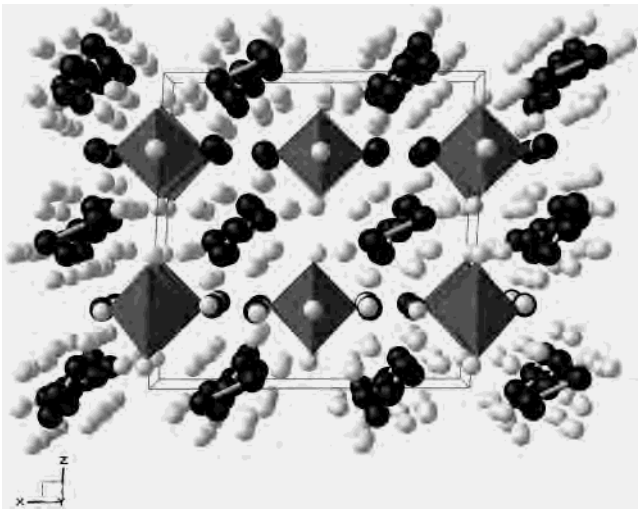

Figure 1. Structure of $Ca_{21}Mn_4Sb_{11}$ viewed in a perspective projection down the *b*-axis. The lightly colored gray spheres are Ca atoms, the black spheres are Sb atoms, and the dark gray polyhedra represent the $[Mn_4Sb_{10}]^{22-}$ linear units. The bonds between atoms of the $[Sb_2]^{4-}$ dumbbells are represented by a gray bar between the Sb atoms.

structure is formed by silicon centered uranium trigonal prisms that share the square face to form rhombic prisms and share the trigonal faces to produce edge sharing columns.[49] Similarly, square face sharing, cobalt centered, trigonal prisms of gallium atoms form the $CoGa_3$ structure, but instead of forming face sharing columns, a corner sharing network is formed.[50] However, these materials are not made up of complex anionic units that occupy the prisms, but are made up of isolated atoms that occupy these sites. The structure of Eu_2Sb_3 and Ca_2As_3 is an example of compounds with a complex anionic network that occupy a prismatic cation environment.[51] They share a common trigonal prismatic AX_2 type defect structure that also links the arrangement of prisms of the AlB_2 type and the α-$ThSi_2$ type.[40,51] Their anionic network, though, contains longer chains of either $[Sb_6]^{8-}$ or $[As_4]^{6-}$ and $[As_8]^{10-}$ anions.

The unique $[Mn_4Sb_{10}]^{22-}$ linear unit is the first example of a linear anionic unit containing four Mn-centered, edge-sharing tetrahedral components and is shown in Figure 2. The relevant Mn−Sb bond lengths, and Sb−Mn−Sb and Mn−Sb−Mn bond angles, are listed in Table 4. The Mn··· Mn distances are provided in the figure. Interestingly, the spatial arrangement of the Mn tetrahedral unit is completely different from the newly reported $Sr_{21}Mn_4Sb_{18}$ compound.[35] In the Sr analogue, a large anionic cluster is made up of eight edge and corner sharing $MnSb_4$ tetrahedral units with a total of six different types of pnicogen anions in the cluster. There are many examples of compounds containing edge sharing chains of two and three tetrahedra including the $[In_2S_6]^{6-}$ anion in $Rb_6In_2S_6$ and $Rb_4In_2S_5$,[52] the $[Al_2Sb_6]^{4-}$

(48) Nyman, H. *J. Solid State Chem.* **1976**, *17*, 75−78.
(49) Wyckoff, R. W. G. In *Crystal Structures*, 2nd ed.; Interscience: New York, 1968; p 344.
(50) Schubert, K. In *Kristallstrukturen zweikomponentigen phasen*; Springer-Verlag: Berlin, 1964; p 301.
(51) Nesper, R.; von Schnering, H. G. *TMPM, Tschermaks Mineral. Petrogr. Mitt.* **1983**, *32*, 195−208.
(52) Deiseroth, H.-J. *Z. Naturforsch.* **1980**, *35b*, 953−958.

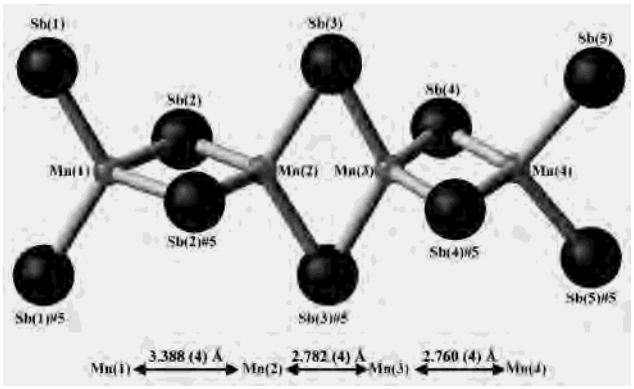

Figure 2. $[Mn_4Sb_{10}]^{22-}$ linear unit showing labels for each of the constituent atoms. The Mn···Mn distances are shown at the bottom of the figure.

Table 4. Selected Bond Lengths [Å] and Angles [deg] for $Ca_{21}Mn_4Sb_{18}$

Sb(1)−Mn(1) × 2	2.803(1)	Sb(8)−Ca(9)	3.081(2)
Sb(2)−Mn(2) × 2	2.717(2)	Sb(8)−Ca(10)	3.333(2)
Sb(2)−Mn(1) × 2	2.801(2)	Sb(9)−Ca(1)	3.024(2)
Sb(3)−Mn(3) × 2	2.802(1)	Sb(9)−Ca(2)	3.282(2)
Sb(3)−Mn(2) × 2	2.882(2)	Sb(9)−Ca(4)	3.059(2)
Sb(4)−Mn(3) × 2	2.762(1)	Sb(9)−Ca(5)	3.828(3)
Sb(4)−Mn(4) × 2	2.845(1)	Sb(9)−Ca(6)	3.023(2)
Sb(5)−Mn(4) × 2	2.745(2)	Sb(9)−Ca(7)	3.398(2)
Sb(6)−Sb(6)	2.866(1)	Sb(9)−Ca(8)	3.367(2)
Sb(6)−Ca(1)	3.462(2)	Sb(9)−Ca(11)	3.0270(8)
Sb(6)−Ca(2)	3.129(2)		
Sb(6)−Ca(3)	3.550(2)	Sb(1)−Mn(1)−Sb(1)	121.48(9)
Sb(6)−Ca(5)	3.494(2)	Sb(1)−Mn(1)−Sb(2)	110.24(2)
Sb(6)−Ca(5	3.527(3)	Sb(1)−Mn(1)−Sb(2)	105.61(2)
Sb(6)−Ca(7)	3.367(2)	Sb(2)−Mn(1)−Sb(2)	102.03(8)
Sb(6)−Ca(7)	3.385(2)	Sb(2)−Mn(2)−Sb(2)	106.52(9)
Sb(6)−Ca(10)	3.180(2)	Sb(2)−Mn(2)−Sb(3)	105.74(2)
Sb(7)−Sb(7	2.895(1)	Sb(2)−Mn(2)−Sb(3)	109.88(2)
Sb(7)−Ca(1)	3.640(2)	Sb(3)−Mn(2)−Sb(3)	118.54(9)
Sb(7)−Ca(3)	3.531(2)	Sb(3)−Mn(3)−Sb(3)	124.29(10)
Sb(7)−Ca(4)	3.116(2)	Sb(4)−Mn(3)−Sb(3)	102.54(2)
Sb(7)−Ca(6)	3.182(2)	Sb(4)−Mn(3)−Sb(3)	102.78(2)
Sb(7)−Ca(8)	3.443(2)	Sb(4)−Mn(3)−Sb(4)	124.07(10)
Sb(7)−Ca(8)	3.486(2)	Sb(4)−Mn(4)−Sb(4)	118.04(9)
Sb(7)−Ca(9)	3.316(2)	Sb(5)−Mn(4)−Sb(4)	110.30(2)
Sb(7)−Ca(9	3.337(2)	Sb(5)−Mn(4)−Sb(4)	107.06(2)
Sb(8)−Ca(2)	3.359(2)	Sb(5)−Mn(4)−Sb(5)	103.09(9)
Sb(8)−Ca(4)	3.333(2)	Sb(5)−Mn(4)−Sb(4)	107.06(2)
Sb(8)−Ca(5)	3.046(2)	Mn(2)−Sb(2)−Mn(1)	75.73(6)
Sb(8)−Ca(6)	3.338(2)	Mn(3)−Sb(3)−Mn(2)	58.58(6)
Sb(8)−Ca(7)	3.068(2)	Mn(3)−Sb(4)−Mn(4)	58.95(6)
Sb(8)−Ca(8)	3.046(2)		

anion in Ba_3AlSb_3,[53] the $[P_2S_6]^{2-}$ anion in $A_2P_2S_6$ (A = K, Cs),[54] and the $[Sn_3Se_8]^{4-}$ anion in $K_4Sn_3Se_8$.[55] In addition, there are many examples of structures containing infinite chains of edge sharing tetrahedra, most notably Li_3FeN_2 which contains infinite chains of edge sharing FeN_2 tetrahedra, $^1_\infty[FeN_{4/2}{}^{3-}]$.[56] However, $Ca_{21}Mn_4Sb_{18}$ is the first example reported to date of a discrete four-membered chain containing edge shared $MnSb_4$ tetrahedra. The Mn−Sb bond distances range from 2.717 to 2.854 Å providing good agreement with the previously reported ternary manganese antimonide phases of $Zn_{0.94}Mn_{0.89}Sb$ (2.736 Å),[57] $EuMn_2Sb_2$ (2.758 Å),[58] $BaMnSb_2$ (2.804 Å),[59] $Ca_{14}MnSb_{11}$ (2.759 Å),[28] and $Sr_{21}Mn_4Sb_{18}$ (2.763−3.007 Å).[35] Deviations from the ideal tetrahedral angle of 109.5° are observed throughout the unit with the maximum angle of 124.3° occurring between Sb(3)−Mn(3)−Sb(3), and the minimum angle of 102.0° occurring between Sb(2)−Mn(1)−Sb(2). In addition, the differences in angle between the extreme ends of the linear unit are quite pronounced with the Sb(1)−Mn(1)−Sb(1) angle being 121.5° and the Sb(5)−Mn(4)−Sb(5) angle being 103.1°. The Mn···Mn distances are 3.388(4) Å Mn1−Mn2, 2.782(4) Å Mn2−Mn3, and 2.760(4) Å Mn3−Mn4. The distances between neighboring Mn atoms approach the elemental Mn metal bond distance of 2.54 Å. However, it is striking that one distance, Mn(1)···Mn(2), is ∼18% longer than the other distances. As mentioned previously, the linear units form columns that extend along the *b*-axis. A single Ca atom, lying directly above all four Mn atoms, separates each unit with the Ca atom lying closer to the larger angle end as shown in Figure 3. This atom appears to influence the angles of the two ends by repelling the Sb atoms of the larger angle and drawing those of the smaller angle closer. The distances from the Ca atom to the Mn atom in the tetramers are not the same. The Mn(4)···Ca(11) distance is 4.507 Å, and the Mn(1)···Ca(11) distance is 3.636 Å. In addition, this Ca atom serves to bridge the trigonal prisms that make up the rows of alternating Sb dumbbells and lone Sb anions. It is also interesting to note that the distance between clusters along the *b*-axis is much longer than the distance between clusters of adjacent columns. The cluster−cluster distances are 5.075 and 4.087 Å, respectively, as measured through the Sb···Sb interactions and are also shown in Figure 3.

Ca atoms surround each anionic unit with edge and face sharing polyhedral cages as shown in Figure 4. A rhombic prism environment encapsulates each Sb dumbbell unit, with each Sb of each dumbbell unit surrounded by Ca atoms in a bicapped, skew, trigonal prism geometry. The isolated Sb ions also occupy bicapped, skew, trigonal prism Ca environments, but they occupy a more distorted trigonal prism than the Sb atoms of the dumbbells. The uncapped, square face of the prism shows the most distortion from the ideal square geometry, with the complementary angles being 105° and 72°. The isolated Sb(6) atoms lie between the Sb(8) and the Sb(4) dumbbells that run along the *b*-axis in the repeating pattern: $[Sb(8)_2]^{4-}-[Sb(6)]^{3-}-[Sb(4)_2].^{4-}$ Because of this arrangement, the uncapped face from two of the Ca prisms for Sb(6) also serve as the parallel face of the rhombic prism planar to the Sb(8) dumbbell bond axis. The peak atoms of the trigonal prism and the two capping Ca atoms from two prisms form the related faces of the Sb(4) dumbbell rhombic prism. This alternating arrangement of Ca prisms stacks along the *b*-axis in combination with the repeating Sb motif, and the Sb(6) prisms are shown to make σ translations between consecutive units forcing consecutive dumbbells to rotate

(53) Cordier, G.; Savelsberg, G.; Schäfer, H. *Z. Naturforsch.* **1982**, *37b*, 975−980.
(54) Brockner, W.; Becker, R.; Eisenmann, B.; Schäfer, H. *Z. Anorg. Allg. Chem.* **1985**, *520*, 51−58.
(55) Sheldrick, W. S. *Z. Naturforsch.* **1988**, *43b*, 249−252.
(56) Gudat, A.; Kniep, R.; Rabenau, A.; Bronger, W.; Ruschewitz, U. *J. Less-Common Met.* **1989**, *161*, 31−36.
(57) Johnson, V.; Jeitschko, W. *J. Solid State Chem.* **1977**, *22*, 71−75.
(58) Ruehl, R.; Jeitschko, W. *Mater. Res. Bull.* **1979**, *14*, 513−517.
(59) Cordier, G.; Schäfer, H. *Z. Naturforsch.* **1977**, *32b*, 383−386.

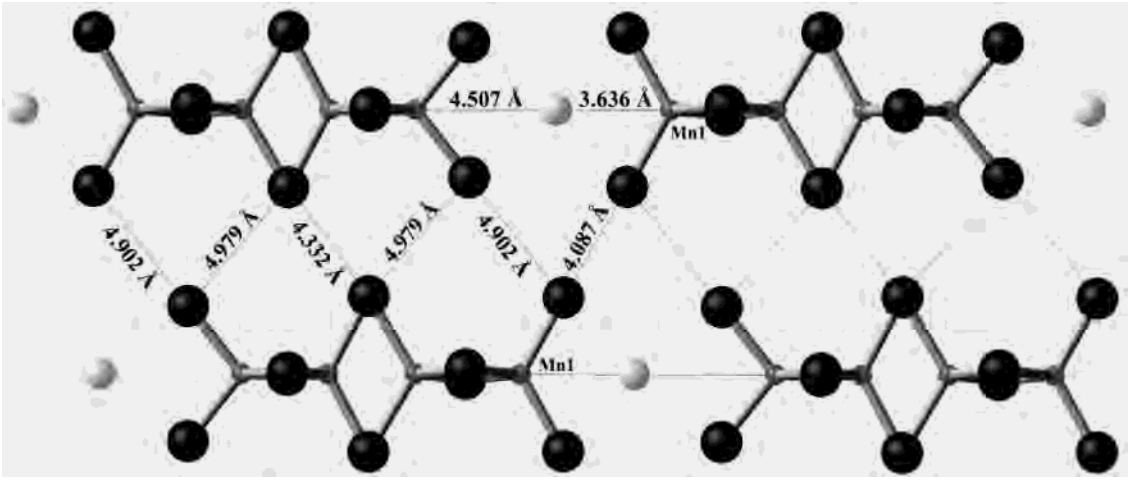

Figure 3. View of the separation between the $[Mn_4Sb_{10}]^{22-}$ linear units. A single Ca atom lies directly between all four Mn atoms, separating each unit, and lies closer to the larger angle end of the linear unit. The Sb···Sb separations between Mn_4 clusters are also shown.

~30° with each translation. The isolated Sb(9) anions translate in a zigzag pattern along the *b*-axis forming a row that alternates with the Sb dumbbell rows along the *c*-axis. Each Sb anion lies part way between the dumbbell and the isolated anion of the next row as a result of sharing of Ca atoms from both the Sb(6) and both of the Sb dumbbells' Ca environment to form bicapped, skew, trigonal prisms. This sharing of Ca atoms results in the zigzag pattern of Sb anions because of the rotation of the dumbbells, and the mirror plane symmetry between consecutive Ca prisms of Sb(6). In addition, this zigzag row lays directly above the row containing the $[Mn_4Sb_{10}]^{22-}$ linear unit.

A more direct structural comparison to our system is found in the Zintl phases of the A_5Z_4 type (A = rare earth or alkaline earth metals; Z = P, As, Si, Ge),[39,43,60,61] the related ternary $A_2^{I}AE_3^{II}X_4$ (A^{I} = Na, K; AE^{II} = Ba, Sr, Eu; X = P, As, Sb) phases,[36,44,45] KBa_4Sb_3O,[36] $Ca_{11}MSb_9$ (M = In, Ga),[37,47] and the $A_{14}MPn_{11}$ (A = Ca, Sr, Ba, Eu, Yb; M = Mn, Zn, Al, Ga, In; Pn = P, As, Sb, Bi) phases.[2,8−34,62] All systems, aside from the $A_{14}MPn_{11}$ compounds, contain dumbbell anions of the $[Sb_2]^{4-}$ type with each atom of the dumbbells occupying a bicapped skew trigonal prism of cations. The $A_{14}MPn_{11}$ compounds contain a $[Pn_3]^{7-}$ trimer instead of the dimer, but each atom of the anion remains consistent in occupying a bicapped skew trigonal prismatic environment. In fact, the most electronegative element in all of these systems occupies the same cationic environment. In addition, aside from the compounds with the $A_2^{I}AE_3^{II}X_4$ structure, all of these systems contain a similar alternating pattern between the single atom anion and the dumbbell anion that produces a related stacking motif to that of the $Ca_{21}Mn_4Sb_{18}$ system. The stacking pattern of the A_5Z_4 compounds differs slightly in that there is an inclusion of an alkaline earth or rare earth centered quasicube in the stacking pattern. In a similar fashion, an O^{2-} centered tetrahedral void disrupts the stacking pattern of Sb anions in KBa_4Sb_3O. These structural changes amount to a replacement of one of the dumbbell units with the respective quasicube or tetrahedral void in the stacking pattern.

The most closely related structure to $Ca_{21}Mn_4Sb_{18}$ in both the cation environment and stacking pattern of the anions is the $Ca_{11}MSb_9$ structure.[47,62] The Ga, Al, and In analogues share the structural features of alternating rows of $[Sb_2]^{4-}$ dumbbell anion and Sb^{3-} anions propagating along a common crystallographic axis (*c*-axis in this case). The closest cation environment is also the same bicapped trigonal prism environment that is observed in $Ca_{21}Mn_4Sb_{18}$. The major difference is the $Ca_{11}MSb_9$ structure contains isolated $[MSb_4]^{9-}$ tetrahedra that form rows along the *c*-axis parallel to the Sb rows as opposed to the rows of $[Mn_4Sb_{10}]^{22-}$. An unusual feature in this row of anions is that a lone Ca atom alternates with each anion in the same way in each structure and lies directly above the central atom(s) of the tetrahedra. Even with this considerable structural difference, the two structures remain remarkably similar. A Mn analogue of the $Ca_{11}MSb_9$ structure has not been reported in the literature to date. This may indicate that the Mn analogue of the $Ca_{11}MSb_9$ system is not thermodynamically stable in the temperature and compositional region that both $Ca_{14}MnSb_{11}$ and $Ca_{21}Mn_4Sb_{18}$ form.

Properties Measurements. Figure 5 shows the magnetization as a function of temperature measurements with various applied fields. The data show a dramatic increase in magnetization at ~52 K indicative of ferromagnetic ordering. The overall shape of the magnetization curves and the sharpness of the transition at 52 K become less well defined with increasing applied field. At a high enough applied field, the ferromagnetic behavior is suppressed and the magnetization data display Curie-like paramagnetic behavior. The data at low applied fields show a significant difference between zero field cooled (ZFC) and field cooled (FC) data that becomes less pronounced above H = 500 Oe. Figure 6 shows the susceptibility as a function of temperature data at H = 1000 Oe, with an inset of the inverse susceptibility data. The

(60) Brechtel, E.; Cordier, G.; Schäfer, H. *Z. Naturforsch.* **1981**, *86 b*, 1341−1342.
(61) Smith, G. S.; Johnson, Q.; Tharp, A. P. *Acta Crystallogr.* **1967**, *22*, 269−272.
(62) Cordier, G.; Schäfer, H.; Stelter, M. *Z. Anorg. Allg. Chem.* **1984**, *519*, 183−188.

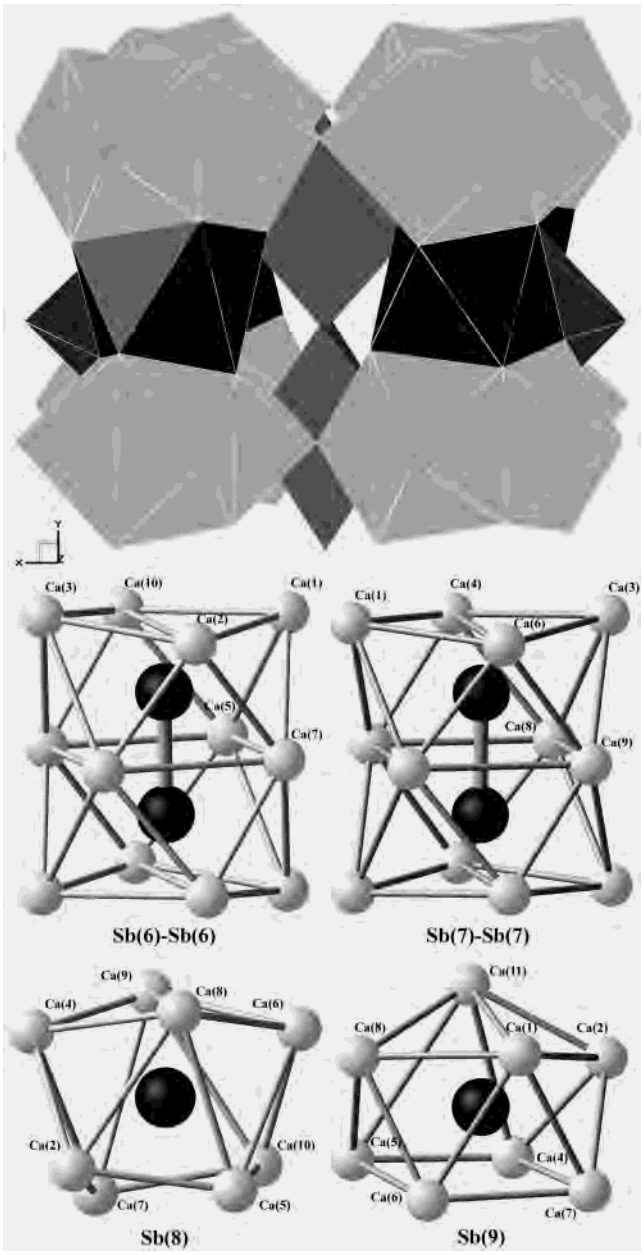

Figure 4. The top portion shows the stacking of the Ca polyhedra that surround each anionic unit with edge and face sharing polyhedral cages. The lighter gray polyhedra represent the rhombic prisms that encapsulate each Sb dumbbell unit, the black polyhedra represent the bicapped, skew, trigonal prisms that surround the isolated Sb^{3-} anions, and the dark gray polyhedra represent the $[Mn_4Sb_{10}]^{22-}$ linear units. The bottom portion shows the constituent Ca atoms that form the polyhedral cages around each of the Sb atoms. Light gray bars are drawn between the Ca atoms as a guide to show how the polyhedra are formed and do not represent real bonds between Ca atoms.

inverse susceptibility demonstrates a distinctive curvature that is most pronounced near the ordering temperature and appears to be a combination of two curves. A similar type of behavior in the inverse susceptibility has been attributed to ferrimagnetic ordering as described by L. Néel in reference to the magnetic oxide ferrites, $MO{\cdot}Fe_3O_4$ (M = Zn, Cd, Fe, Ni, Cu, Co, Mg).[63] The high temperature data (54−300 K) can be fit using a ferrimagnetic Curie model assuming two

(63) Kittel, C. In *Introduction to Solid State Physics*, 7th ed.; John Wiley and Sons: New York, 1996; pp 458−462.

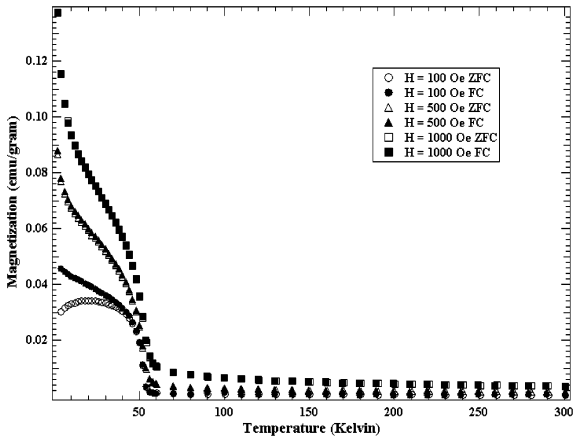

Figure 5. Temperature dependent magnetization curves (emu/g) of $Ca_{21}Mn_4Sb_{18}$ at H_a = 100, 500, and 1000 Oe. Zero field-cooled (ZFC) and field-cooled (FC) data are shown.

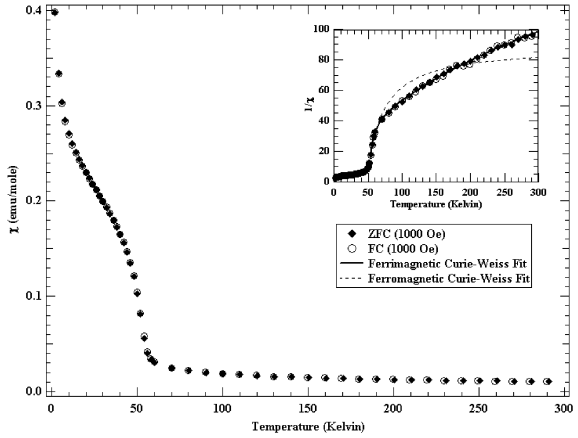

Figure 6. Temperature dependent magnetic susceptibility data (emu/mol) of $Ca_{21}Mn_4Sb_{18}$ at H_a = 1000 Oe for both ZFC and FC measurements. The inset shows a plot of the inverse susceptibility for the same data. A fit of the susceptibility data from 54 to 300 K is shown for both a ferrimagnetic model (—) and a modified Curie−Weiss model (- - -) in the inset.

separate magnetic sites as a first approximation, $\chi = [(C_A + C_B)T - 2\mu C_A C_B]/(T^2 - T_C^2) + \chi_0$, and yield a T_c = 51.85(6) K. The fit of the susceptibility data is shown in the inset with a solid line in Figure 6, and the parameters are provided in Table 5. For comparison, the data in the paramagnetic region has also been fit using a modified Curie−Weiss model, $\chi = (C/T - T_c)$, and yield a similar T_c = 48.0(9) K. The parameters obtained for this fit are also provided in Table 5. Comparing χ_o from the two fits, the χ_o obtained from the ferrimagnetic model is more reasonable with the χ_o obtained from the Curie−Weiss fit being too large to be reasonable. The Curie constants provided by the ferrimagnetic model provide an effective moment that is most consistent with one Mn^{3+} moment, and the experimental value for μ_{eff} (4.04(2) μ_B) is much smaller than the calculated value for four Mn^{2+} ions (11.8μ_B). The Curie constant from the Curie−Weiss model is also not consistent with four Mn ions in any state but is equivalent to a single d^1 moment or a Mn^{6+}-like ion (μ_{eff} = 1.43(9) μ_B).

The simplest models to describe this system are if the four Mn moments are not coupled, giving rise to 11.8 μ_B/Mn_4 cluster, or if the four Mn moments couple strongly giving rise to antiferromagnetic alignment, providing 0 μ_B/Mn_4

Table 5. Magnetic and Resistivity Data

Magnetic Data			
ferrimagnetic Curie−Weiss fit		ferromagnetic Curie−Weiss fit	
C_A[a]	0.853(7)	C[c]	0.25(3)
C_B[a]	1.18(2)	T_c[c] (K)	48.0(9)
μ[a]	48.50(2)	χ_o[c] (emu/mol)	0.0113(5)
T_c[a] (K)	51.85(6)	μ_{eff}[d] (μ_B)	1.43(9)
χ_o[a] (emu/mol)	0.0043(2)		
μ_{eff}[b] (μ_B)	4.04(2)		
Resistivity Data			
E_a[e] (eV)		0.159(2)	
ρ_o[e] (Ω-cm)		4.11(7)	

[a] Obtained from fitting the inverse susceptibility data for $H_a = 1000$ Oe from 54 to 300 K with the equation $\chi = [(C_A + C_B)T - 2\mu C_A C_B]/(T^2 - T_c^2) + \chi_o$. [b] Calculated from the equation $\mu_{eff} = \sqrt{7.99(C_A+C_B)}$. The theoretical value for 4 Mn^{2+} ions is 11.8 μ_B from the equation $\mu_{eff}^2 = 4\mu_{Mn^{2+}}$. [c] Obtained from fitting the inverse susceptibility data for $H_a = 1000$ Oe from 54 to 300 K with the equation $\chi = (C/T - T_c) + \chi_o$. [d] Calculated from the equation $\mu_{eff}^2 = \sqrt{7.99C}$. [e] Obtained from fitting ln ρ data from 100 to 300 K with the equation ln $\rho = (E_a/2k_BT) - \rho_o$.

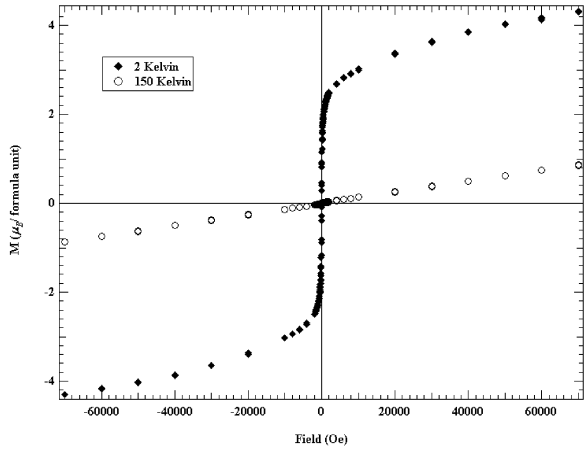

Figure 7. Hysteresis loop of $Ca_{21}Mn_4Sb_{18}$ at 2 and 150 K.

cluster. The antiferromagnetic alignment would be the most probable if the Mn^{2+} ions were equally spaced with similar Mn−Sb−Mn angles. The Mn···Mn distances in the $[Mn_4Sb_{10}]^{22-}$ unit are 3.388(4), 2.782(4), and 2.760(4) Å. In addition, the Mn−Sb−Mn angle of about 75° between Mn(1) and Mn(2) differs significantly from the angle of about 58° observed for the Mn−Sb−Mn angle between Mn(2), Mn(3), and Mn(4). This configuration gives rise to a situation where three of the Mn^{2+} moments might be antiferromagnetically aligned, and the fourth Mn^{2+} moment is only weakly coupled. Therefore, although aligned anti to its nearest neighbor, the magnetic ordering of the cluster is presumed to be ferrimagnetic. This would be consistent with using a two magnetic site model already described for the paramagnetic regime as well.

Figure 7 shows hysteresis loops at 2 and 150 K showing no measurable hysteresis. Saturation magnetization has not been reached even at 7 T. The fact that saturation is not achieved may be due to the fact that these measurements are on a single crystal and anisotropy may be important. The maximum magnetization value (μ_{max}) of a little more than 4 μ_B/formula unit is much lower than what would be expected for complete ferromagnetic ordering of four Mn^{2+}, d^5 ions

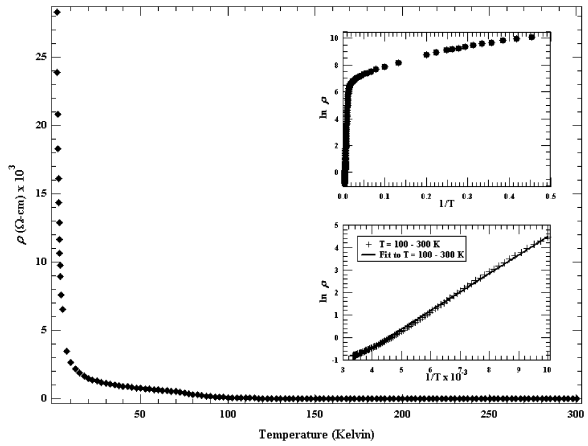

Figure 8. Temperature dependent resistivity data of a single crystal of $Ca_{21}Mn_4Sb_{18}$. The top inset shows a plot of ln ρ vs $1/T$ for the entire data set, and the bottom inset shows a plot of just the region from 100 to 300 K with the dark line representing the fit using the equation $(E_a/2k_BT) - \rho_o$.

(expected $\mu_{sat} = 20\ \mu_B$). Long range ferromagnetic ordering must be between Mn_4 clusters. This model suggests that partial cancellation of spin in a ferrimagnetic model results in a total spin of 4 μ_B/Mn_4 cluster in the ordered regime. The cluster can couple to the next by means of short Sb··· Sb intercluster interactions as shown in Figure 3 or by conduction electrons. With recent calculations on $Ca_{14}MnBi_{11}$ and $Ba_{14}MnBi_{11}$, and XMCD results on $Yb_{14}MnSb_{11}$ showing spin density on both Mn and Pn in the $MnPn_4$ cluster, it is possible that a much more complex spin situation is present in this unusual structure.[18,29]

Measurements of resistivity as a function of temperature were carried out to further investigate the mechanism for ordering in this system. A plot of resistivity as a function of temperature for a single crystal is shown in Figure 8. The data show saturation effects at low temperature, typical of semiconductors. A plot of ln ρ versus $1/T$ is nearly linear over the temperature range 100−300 K, and an activation energy of 0.159(2) eV is calculated from the equation ln $\rho = (E_a/2k_BT) - \rho_o$.

Semiconducting behavior is expected for traditional Zintl phases as they are generally regarded as closed-shell compounds following traditional Zintl−Klemm electron counting rules, but it is unexpected to observe semiconducting and ferromagnetic properties coexisting since, for most compounds, the exchange of spins leads to antiferromagnetic coupling. The simultaneous occurrence of ferrimagnetic and semiconducting behavior is well-known among many transition metal oxide and non-oxide perovskite systems,[64−70] and has been observed in the ternary chromium chalcogenides ACr_2X_4 (A = C, Hg, Cu, Zn, Fe, Co, Mn; X = S, Se).[71−73] Goodenough, Kanamori, and Anderson have explained this

(64) Mizokawa, T.; Khomskii, D. I.; Sawatzky, G. A. *Phys. Rev. B* **2000**, *63*, 1−5.
(65) Koo, H.-J.; Whangbo, M.-H. *J. Solid State Chem.* **2000**, *151*, 96−101.
(66) Grant, J. B.; McMahan, A. K. *Phys. Rev. Lett.* **1991**, *66*, 488−491.
(67) Tokura, Y.; Nagaosa, N. *Science* **2000**, *288*, 462−468.
(68) Weht, R.; Pickett, W. E. *Phys. Rev. B* **2001**, *65*, 1−6.
(69) Feldkemper, S.; Weber, W.; Schulenburg, J.; Richter, J. *Phys. Rev. B* **1995**, *52*, 313−323.
(70) Kuang, X.-Y.; Zhou, K.-W. *Physica B* **2001**, *307*, 34−39.

type of ferromagnetism as occurring by exchange coupling of symmetry appropriate ground- and excited-state orbitals of the magnetic ions.[74−76] They also describe this type of ferromagnetic coupling as occurring simultaneously with the cooperative Jahn−Teller effect as is described for the in-plane ferromagnetic coupling of K_2CuF_4.[69]

Ferromagnetic ordering of discrete clusters is rare, but the small band gap and possible spin polarization of the Sb may provide a mechanism. Each of the $MnSb_4$ tetrahedra in the $[Mn_4Sb_{10}]^{22-}$ linear unit of $Ca_{21}Mn_4Sb_{18}$ show deviations in the Sb−Mn−Sb angles away from the ideal tetrahedral angle of 109.4°. This type of distortion has also been observed in the MPn_4 tetrahedra of the related $A_{14}MPn_{11}$ compounds and is attributed to a Jahn−Teller distortion.[22] In addition, the Mn−Sb−Mn angles differ significantly from one another as stated previously. It is possible that the magnetic coupling of $Ca_{21}Mn_4Sb_{18}$ arises from interplay between the spin and orbital degrees of freedom of Mn and Sb as promoted by a Jahn−Teller type distortion of the $MnSb_4$ tetrahedra in an analogous fashion to that described by Goodenough, Kanamori, and Anderson.[74−76] In addition, the close proximity between the Sb atoms bonded to Mn(1) of adjacent Mn_4 clusters as shown in Figure 3 provides a possible pathway for the magnetic interactions to occur along. A similar type of interaction in $BaVS_3$ has been described using first principles and tight-binding electronic structure calculations for the orbital interactions associated with the short S···S interactions within each VS_3 chain and between adjacent VS_3 chains.[77] It is likely that the mechanism describing the magnetic interactions is complicated, and a detailed theoretical study is necessary to understand the interaction of the local moments.

Summary

A new addition to the family of Mn containing transition metal Zintl phases has been synthesized. The structure of $Ca_{21}Mn_4Sb_{18}$ complements the recently reported $Sr_{21}Mn_4Sb_{18}$ phase that is compositionally identical but differs substantially in its structure. This new structure contains noninfinite, discrete linear units of Mn-centered, edge sharing tetrahedral units in a $[Mn_4Sb_{10}]^{22-}$ unit, and also retains the well-known $[Sb_2]^{4-}$ Zintl anion, exhibiting a consistency within the cationic framework with other Zintl phases possessing this anionic unit. Temperature dependent magnetization shows a ferromagnetic transition temperature at ∼52 K which is suppressed with increasing magnetic field and is best described with a ferrimagnetic model indicating a more complex type of magnetic interaction. Temperature dependent resistivity shows that this compound is a semiconductor with an activation energy of 0.159(2) eV (100−300 K).

Acknowledgment. The initial investigations of this system were performed by D. M. Young and E. A. Axtell, III. We thank P. Klavins for technical assistance and R.N. Shelton for the use of the SQUID magnetometer. This research is funded by the National Science Foundation Grant DMR-9803074, 0120990, and the Materials Research Institute through Lawrence Livermore National Laboratory.

Supporting Information Available: X-ray crystallographic file in CIF format for the structure of $Ca_{21}Mn_4Sb_{18}$. This material is available free of charge via the Internet at http://pubs.acs.org.

IC020530R

(71) Menyuk, N.; Dwight, K.; Arnott, R. J.; Wold, A. *J. Appl. Phys.* **1966**, *37*, 1387.
(72) Baltzer, P. K.; Lehmann, H. W.; Robbins, M. *Phys. Rev. Lett.* **1965**, *15*, 493−495.
(73) Tsurkan, V.; Fita, I.; Baran, M.; Puzniak, R.; Samusi, D.; Szymczak, R.; Szymczak, H.; Klimm, S.; Klemm, M.; Horn, S.; Tidecks, R. *J. Appl. Phys.* **2001**, *90*, 875−881.
(74) Goodenough, J. B. *J. Phys. Chem. Solids* **1958**, *6*, 287.
(75) Kanamori, J. *J. Phys. Chem. Solids* **1959**, *10*, 87.
(76) Anderson, P. W. *Phys. Rev. Lett.* **1959**, *115*, 2−13.
(77) Whangbo, M.-H.; Koo, H.-J.; Dai, D.; Villesuzanne, A. *J. Solid State Chem.* **2002**, *165*, 345−358.